AAS (Pre-print) 22-134

DESIGN OF THE ON-BOARD IMAGE PROCESSING OF THE MILANI MISSION

M. Pugliatti*, V. Franzese†, A. Rizza*, F. Piccolo*, C. Bottiglieri‡, C. Giordano† , F. Ferrari§, and F. Topputo¶

Milani is a 6U CubeSat that will visit the Didymos binary system as part of the Hera mission. Its objectives are both scientific and technological: to study and characterize the asteroid environment, and to demonstrate the use of CubeSat technologies for interplanetary missions. The latter includes optical-based autonomous navigation algorithms in a close-proximity environment, which are enabled by robust image processing functions. In this work, for the first time, the design of the image processing of Milani is described in detail. Its algorithmic core is divided among two blocks: the blobs characterization and the observables extraction. The former one extracts low-level optical observables while distinguishing the primary from the secondary of the Didymos system. The latter processes the input of the previous block to generate higher-level observables such as the center of figure, the range, and the phase angle. These estimates are generated thanks to data-driven functions which are tuned on a global dataset representative of the geometric conditions which Milani would encounter during its mission. After a detailed description of its functionalities, the image processing is tested on two datasets representative of the nominal mission phases: the far range phase and the close range phase. After the characterization of the various algorithms, it is demonstrated that Milani's image processing is capable of robustly generating a set of optical observables to be used on-board by the GNC and the rest of the CubeSat.

INTRODUCTION

Small bodies in the Solar System represent the current frontier in space exploration. Various missions such as Rosetta [1], Hayabusa 1 [2] and 2 [3], and Osiris-Rex [4] have been launched towards these targets, while others are planned for the future [5, 6, 7]. When arrived in the proximity of a small body, deep-space CubeSats offer the advantage of diversifying and complementing large spacecraft missions [8]. Indeed, they can be exploited as opportunistic payloads to be deployed in situ, once the main spacecraft has reached its target. An example is given by the AIDA (Asteroid Impact and Deflection Assessment) collaboration between NASA and ESA to study and characterize an impact with the Didymos asteroid system [9]. As part of this collaboration, NASA launched the DART (Double Asteroid Redirection Test) kinetic impactor spacecraft [10], whose impact with the secondary asteroid of Didymos will be observed and characterized by LICIACube in autumn 2022 [11]. As part of this cooperation, ESA will launch in October 2024 the Hera mission [6] together with two deep-space CubeSats, namely Juventas [12] and Milani [13, 14, 15], to study and characterize the system.

Autonomous Optical Navigation (OpNav) is an enabling technology for present and future exploration missions. Such a technique exploits an Image Processing (IP) method to extract optical observables and then use them to generate a state estimate with associated uncertainties. Often the state estimate is refined through filtering techniques, which combine information from the dynamics with an observation model to achieve

*PhD student, Department of Aerospace Science and Technology, Politecnico di Milano, mattia.pugliatti@polimi.it
†PostDoc fellow, Department of Aerospace Science and Technology, Politecnico di Milano
‡Research assistant, Department of Aerospace Science and Technology, Politecnico di Milano
§External collaborator, PostDoc fellow, University of Bern, Physics Institute
¶Full professor, Department of Aerospace Science and Technology, Politecnico di Milano

much higher accuracy than from IP alone. Since images can be inexpensively generated on-board with low-cost and low-mass sensors, OpNav is experiencing a growing interest. This is particularly relevant for CubeSat missions, which are often tightly constrained in terms of mass and power. In the case of proximity to small-bodies, OpNav can be exploited to reduce costs by enabling autonomous system and unlocking the capabilities to perform critical operations. By linking OpNav capabilities with guidance and control algorithms, autonomous GNC systems can be foreseen in the near future in self-exploring missions with reduced or complete absence of humans-in-the-loop. Within this context, the design of an accurate and robust IP algorithm is of paramount importance for a vision-based autonomous GNC system.

In this work, for the first time, the design of the IP algorithm that will be used in the Milani mission is described in detail and its performance are characterized on two nominal phases of the mission. The case of Milani is particularly challenging due to the binary nature of the Didymos system, which requires tailored solutions and some intrinsic robustness of the IP. Due to the associated high uncertainty about the system, the IP is designed to be highly tunable using its many configuration parameters. Moreover, the IP of Milani is making use of data-driven functions, pivoting on the fact that new data about the system could be provided before release by the DART and Hera missions.

The rest of the paper is organized as follows. First, the main characteristics of the Milani mission are briefly illustrated. This is followed up by a detailed discussion about the design of the IP. After such discussion, the performances of the IP are illustrated in the two main phases of the mission. Finally, some conclusions about the current developmental stage of the IP are discussed as well as some points for future improvements.

MILANI MISSION

Milani is a 6U CubeSat that will characterize the Didymos binary system and its close environment. The primary and secondary bodies of the system are called Didymos and Dimorphos (for simplicity, also referred to as D_1 and D_2 in this work). The first has an estimated diameter of 780 m, the latter of 170 m. Milani's objectives are both scientific and technological: to map and study the composition of D_1 and D_2, and to demonstrate CubeSat technologies in deep space. Milani is designed with orbital maneuvering capabilities and attitude control and will carry the ASPECT [16] visual and near-IR imaging spectrometer and VISTA thermogravimeter [17] to characterize the dust environment around the system. The CubeSat is currently designed to host a NavCam (21×16 deg FOV, with a 2048×1536 pixels wide sensor mounted co-axially to ASPECT), a lidar, Sun sensors, a star-tracker, and an IMU.

Milani will be hovering in the Didymos system and will perform the required scientific observations during two main phases: The Far Range Phase (FRP) and the Close Range Phase (CRP). The FRP lasts roughly 21 days while the CRP 28 days. The FRP exhibits symmetrical arcs that develop within 8-14 km from the asteroids. On the other hand, the CRP exhibits asymmetrical arcs within 2-11 km from the asteroids. The NavCam characteristics have been tuned together with the ASPECT requirements to make sure that images can be obtained with D_1 fully resolved during scientific acquisitions and for on-board navigation, avoiding the use of mosaics.

Milani is designed with semi-autonomous capabilities enabled by innovative image processing and autonomous navigation components paired with traditional guidance and control logic. Milani's on-board navigation strategy relies on optical observables of D_1 extracted from images and then used in on-board filters. To do so a robust, simple, and accurate IP method is needed. For the case of Milani, the IP needs to provide reliable data about D_1 for navigation, but at the same time to be able to distinguish D_2 in the image for pointing purposes. This stems from the consideration that D_1 being the largest, most visible, and regular body, it would be simpler and more robust to use for navigation. On the other hand, D_2 being the focus of the mission is important to be able to distinguish D_2 from D_1 in the image to eventually be able to point towards it for scientific acquisitions.

Various works in the literature are sprouting illustrating different aspects of the Milani mission. The most relevant ones are briefly listed here for the interested reader to provide context for what is presented and what is omitted in this work. The process of designing close-proximity operations in a binary asteroid system is discussed at length in [14] while the preliminary mission analysis and GNC design of Milani, which

constituted the proposal and phase 0 of the mission, are illustrated in [13]. A partial description of the IP can be found in [18], which also contains a performance assessment of one of the algorithms presented in this work against machine learning methods. This same algorithm is tested in a Hardware-In-The-Loop facility in [19], illustrating its robustness to varying conditions. A detailed overview of the mission and its semi-autonomous vision-based GNC system is illustrated in [15] while in [20] the important relationship between the trajectory design and orbit determination processes is shown. The interested reader is also directed to [17, 16] for details about VISTA and ASPECT, respectively.

Milani consortium is composed by entities and institutions from Italy, Czech Republic and Finland. Consortium Prime is Tyvak International, responsible for the whole program management and platform design, development, integration, testing and final delivery to the customer. Politecnico di Milano, and in particular the DART* team, is responsible for the Mission Analysis and GNC. Milani successfully achieved the Preliminary Design Review (PDR) in Summer 2021 and is currently in phase-C.

IP

The IP software of Milani is composed of 5 blocks, as it is illustrated in Figure 1. The input is made by a combination of signals containing both data (images, readings from other sensors, variables from higher systems) and configuration parameters. The latter are currently represented by a set of 23 parameters which are used to tune the performance of the IP. For simplicity, these are not explicitly represented in the architectures nor illustrated in this work. The output of the IP is a state vector whose elements are summarized in Table 1. The *PreProcessing* and *PostProcessing* blocks handle the interface between the IP and the rest of the on-board software, performing internal logic checks and generating validity or other types of flags. The *State Machine* is the decision-making core of the IP. On the basis of the validity and operative flags communicated from outside or generated internally, it decides which of the 4 operative modes to use. From the highest to the lowest, it can operate in the SSWCOB, WCOB, COB, or NOP mode. The first three are associated with the choice of the main algorithm to use in the *Observables Extraction* block while the latter is a mode in which no operations are performed. The algorithmic core of the IP resides in the *Blobs Characterization* and *Observables Extraction* blocks, which sequentially process an image and generate optical observables to be used by the rest of the GNC. The task of the *Blobs Characterization* is to generate low-level optical observables from a simple blob analysis while also distinguishing between D_1 and D_2. The task of the *Observables Extraction* is to further process the image content around D_1 to generate a more sophisticated set of observables.

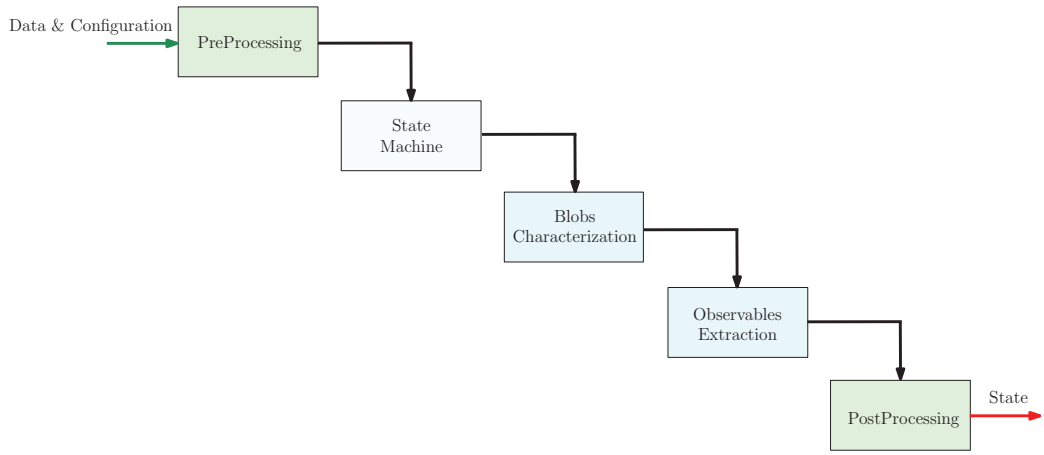

Figure 1: High level architecture of the IP.

The IP software is set to run on-demand within the Milani's NavCam whenever a new image is available.

*https://dart.polimi.it/, last accessed: 27th of January, 2021.

Currently, the IP is designed in Simulink* in order to be easily interfaced with the rest of the GNC [15]. Exploiting the auto-coding capabilities of Simulink, the IP code will be translated into C to be deployed as on-board software.

Table 1: Output of the IP of Milani.

Name	Symbol	Description
number of bodies	f	Number of bodies detected in the image
CoF of D_1	$(CoF)_{D_1}$	Estimated Center of Figure of D_1
CoF of D_2	$(CoF)_{D_2}$	Estimated Center of Figure of D_2
phase angle	Ψ	Estimated phase angle from D_1
range	ρ	Estimated range from D_1
ip mode	γ	Operative mode of the IP
consistency flag	ν_1	Consistency flag on the output of the IP
asteroid detection	ν_2	Detection flag of a body in the image

Blobs Characterization

This block has a twofold purpose: to distinguish between D_1 and D_2, and to generate low-level optical observables. The architecture of the *Blobs Characterization* block is schematized in Figure 2.

At first, the image is binarized using the Otsu method [21] (default choice) or via an arbitrary binary threshold. Morphological operations such as opening or closing are then applied to the binary image. Thanks to this step, the number of detected blobs in the image is reduced, which is helpful in the following blob analysis. The analysis is performed only on the group of pixels larger than a predefined threshold (this is done to remove small image artifacts) and generates several geometric properties of interest for each blob: e.g., area, bounding box characteristics (Γ), centroid coordinates (CoB), eccentricity (e) and major axis length (δ) of the ellipse fitted to the blob of pixels, as illustrated in Figure 2. The output of the blob analysis is first used in the object recognition algorithm to distinguish D_2 from D_1, which is designed as follows:

1. The blobs of pixels are ordered in ascending order based on their areas.
2. The blob with the biggest area is labeled as D_1. Its key geometric properties are saved. All other blobs are listed as potential candidates of D_2.
3. Γ, the bounding box around D_1, is expanded by an arbitrary factor in all directions in the image plane. The expanded bounding box Γ^{ex} is created.
4. The remaining blobs of pixels which are within Γ^{ex} are removed from the list of D_2 candidates. These could be false positive identifications of D_2 given by local areas in the terminator region of D_1.
5. The biggest blob outside Γ^{ex} is therefore labeled as D_2. Its key geometric properties are saved.
6. The number of asteroids detected in the image, f, and the centroid of D_2, $(CoF)_{D_2}$, are passed as output of the IP while the other geometrical properties about D_1 are passed to the *Observables Extraction* block.

Note that the CoF of D_2 is designed to be equivalent to its CoB. This could not be the case (depending on the operative mode γ) for the CoF of D_1, as it is illustrated in the next section.

Observables Extraction

This block takes as input the Region of Interest (ROI) of the image around D_1 identified by Γ^{ex}, its geometrical properties computed in the *Blobs Characterization* block, and external data to compute high-level optical observables with algorithms that are more sophisticated than a simple blob analysis. The architecture of the *Observables Extraction* block is schematized in Figure 3.

*https://www.mathworks.com/products/simulink.html, last accessed: 18th November 2021.

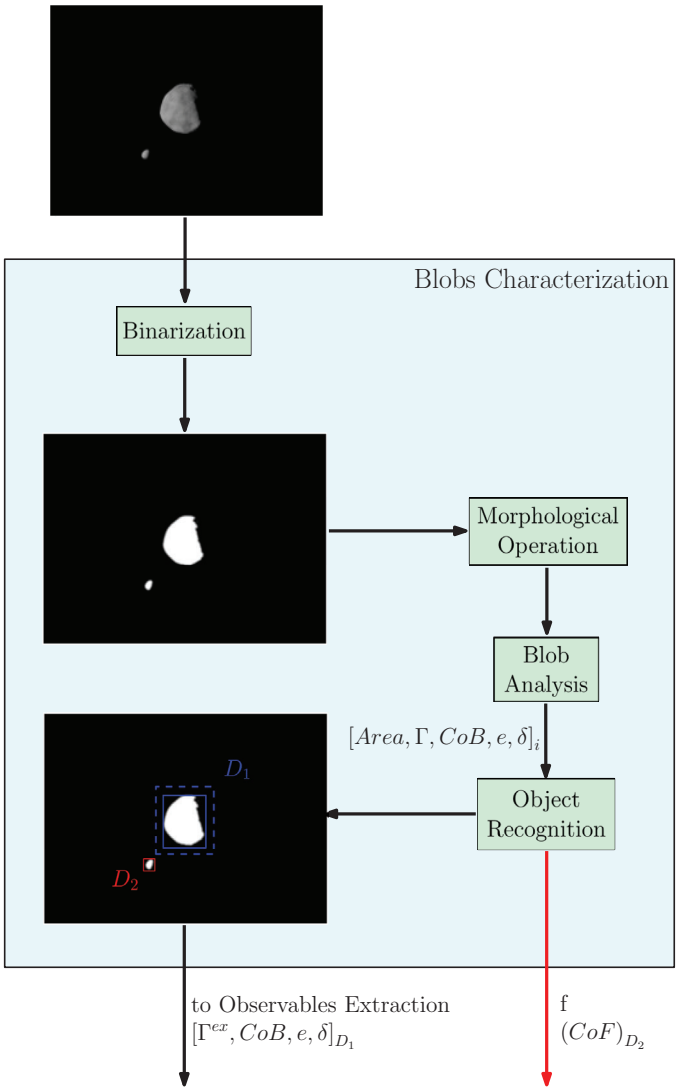

Figure 2: Architecture of the Blobs Characterization block. The red arrow represents the output of the block.

Independently from γ, the range from D_1 is estimated by using a simple apparent diameter relationship:

$$\rho = \frac{R_{D_1}}{\tan\left(\frac{\delta \cdot ifov}{2}\right)} \tag{1}$$

where R_{D_1} is the radius of D_1 in meters, δ is the major axis length of the blob of pixels and $ifov$ is the sensor's instantaneous FOV. The remaining output of the block is computed based on the operative mode γ. These are entangled with the 3 main algorithms that can be used to compute the CoF of D_1 and the phase angle Ψ: the Center Of Brightness (COB), Weighted Center Of Brightness (WCOB), and the Sun Sensor Weighted Center Of Brightness (SSWCOB). Each of these constitutes a branch within the *Observables Extraction* block, as it is illustrated in Figure 3.

The COB branch does not generate an estimate of Ψ, but generates only an estimate of the CoF of D_1. It does that with a simple centroid formula (the one computed from the blob analysis in the *Blobs Characterization* block), which suffers from biases given by the irregular shape of the asteroid and the phase angle.

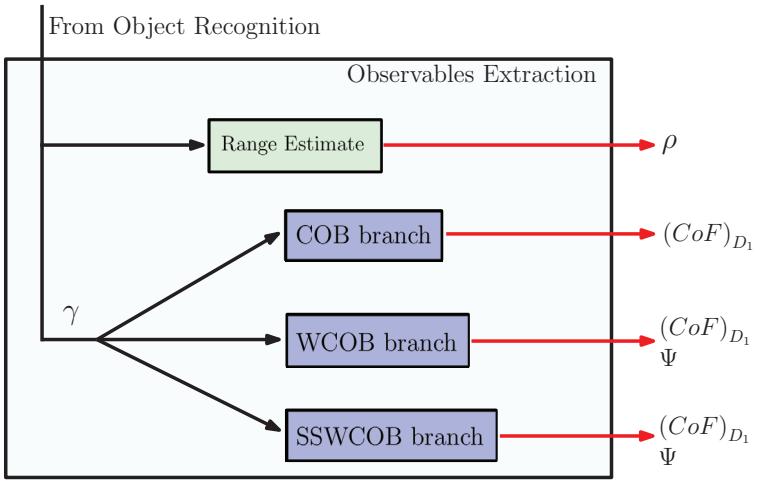

Figure 3: Architecture of the Observables Extraction block. The red arrow represents the output of the block.

To rectify them, a correction term is introduced in the WCOB and SSWCOB branches. In the former one, this term is purely data-driven and computed via quantities extracted from the image, while in the latter it is computed with a mix of data from the Sun sensor and processed from the image.

To design, train and validate the WCOB and SSWCOB methods, a global database is generated, referred to as DB_0. The setup used is the same as the one considered in [18]. DB_0 collects a large statistical sample of $10,000$ images of the Didymos binary system seen from different geometric configurations. It comprehends randomly generated points between 4 km and 14 km with azimuth angle between -95 deg and + 95 deg and elevation between -45 deg and +45 deg with respect to a reference frame co-planar with the orbital plane of the secondary. These conditions are representative of a mission designed to actively observe an asteroid from the illuminated side. During the generation of the database, the angular position of the secondary with respect to the primary is changed randomly, constraining the secondary to be tidally locked with the primary.

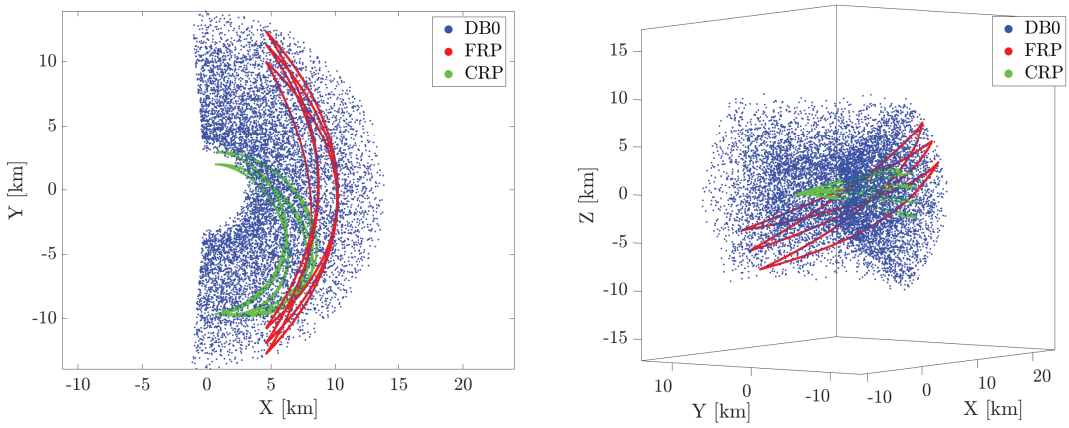

Figure 4: Cloud of points of DB_0 used for training/validation (blue) and points used for testing (red and green), representing the FRP and CRP.

For simplicity, ideal pointing towards the CoM of the primary is assumed and the images are obtained with the NavCam characteristics but without noise. Moreover, the X axis of the NavCam is aligned with

the equatorial plane of the binary system, assuming that the Z axis represents the boresight direction and the X and Y axes are respectively the ones associated with the longest and shortest size of the sensor. The shape models used are enhanced versions of the current ones for the Didymos system. They are processed with procedural changes and re-mesh to simulate roughness and albedo variations with cloud and Voronoi patterns. A 10 m crater is also added on the secondary (which in this work is considered only as a disturbing element) to simulate the DART impact. The algorithm in each branch is now discussed in detail.

Using these settings both the training dataset (DB_0, composed of 10000 images) for the data-driven functions and the testing datasets (FRP and CRP, composed respectively of 12102 and 16020 images) are generated and used to train, validate, and test the image processing software. A representation of the three datasets is visible in Figure 4.

COB

The COB algorithm is a simple, traditional, robust, and well-known method used to estimate the centroid of a figure by its center of brightness. The CoB is computed over the binary image in the blob analysis performed in the *Blobs Characterization* block using the following equation:

$$CoB_x = \frac{\sum_{i,j=1}^{N} I_{ij} x_{ij}}{\sum_{i,j=1}^{N} I_{ij}} \quad CoB_y = \frac{\sum_{i,j=1}^{N} I_{ij} y_{ij}}{\sum_{i,j=1}^{N} I_{ij}} \tag{2}$$

where I_{ij} is the logic value that determines if the pixel (x_{ij}, y_{ij}) is illuminated or not, whereas CoB_x and CoB_y are the components in pixel of the CoB.

WCOB

The COB suffers a bias given by the irregular shape of the body and by high phase angles. To overcome the latter, analytical scattering laws can be used [22, 23]. In the case of the IP of Milani, data-driven scattering laws are applied as variants of the COB algorithm.

The WCOB corrects the CoB by a scattering law derived empirically through data from the irregular body considered. The main goal of the WCOB is to generate a correction vector on the image plane that pushes the CoB towards the CoM, assuming a body with constant density. The WCOB is constituted by two pipelines, as it is possible to see in Figure 5. These are responsible for the computation of the magnitude and orientation components of the correction term to apply to the CoB of D_1. The starting points are two ROIs around D_1 taken from the grayscale and binary version of the image.

Flowing first on the pipeline computing μ, is possible to determine thanks to the DB_0 dataset that a relationship exists between the eccentricity of the blob of pixels associated to D_1 and Ψ. To describe this relationship, a second-order polynomial is used to fit the data represented in Figure 6 in the least square sense:

$$\Psi(e) = p_2 e^2 + p_1 e + p_0 \tag{3}$$

where p_0, p_1, and p_2 are coefficients evaluated from the fit, while e is the eccentricity of the blob of pixels associated with D_1. As illustrated in Figure 6, the Ψ estimated with Equation 3 would be capable to provide a rough estimate which is more precise at higher values of the phase angle. The fit error follows a Gaussian distribution with mean $\mu_\Psi = 0$ deg and standard deviation $\sigma_\Psi = 6.383$ deg.

Following a similar approach, it is also observed that a relationship could be defined between Ψ, δ and the difference between the CoF and CoB, the latter being the magnitude of the correction term μ. The relationship is described by a fifth-order polynomial surface which is once again fit in the least squares sense:

$$\mu(\Psi, \delta) = \sum_{\substack{i=0,\cdots,5 \\ j=0,\cdots,5 \\ i \cdot j \leq 6}} p_{ij} \Psi^i \delta^j \tag{4}$$

Switching to the second pipeline of the WCOB algorithm, Φ is computed starting from the ROI of the grayscale image around D_1. A filter is applied to exacerbate differences between the soft and sharp gradient

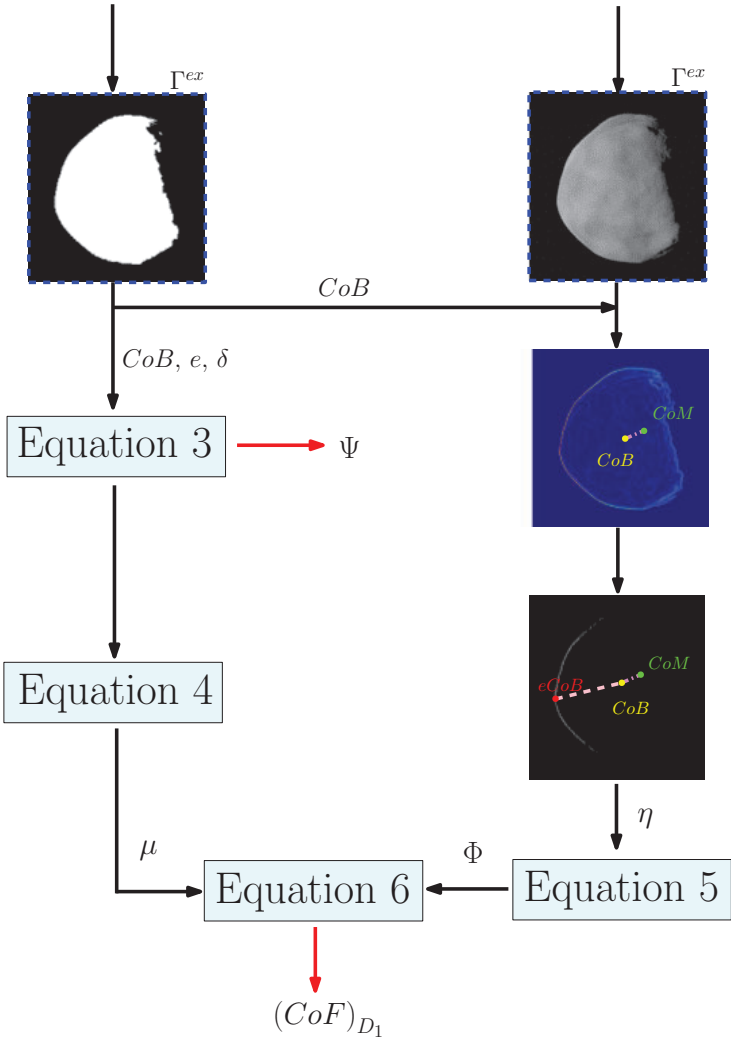

Figure 5: Architecture of the WCOB algorithm. The red arrow represents the output of the algorithm.

over the terminator and edge of the asteroid. To do so, in this work a Sobel filter is used. Once the activation map of the Sobel filter is generated, an arbitrary factor is used to threshold the map by a fraction of the maximum value present in it. The generated binary map is then analyzed and the CoB of the largest blob of pixels, associated with the region on the edge of D_1, is computed. This is referred to as $eCoB$ (edge CoB) and is used to provide an information about the lighting conditions on the asteroid. The CoM, CoB and $eCoB$ are illustrated in one case in Figure 5. From this figure, it is possible to see that the line connecting the $eCoB$ with the CoB can be used to estimate the orientation of the line connecting the CoB with the CoM, which represents the ultimate orientation at which the correction term of the WCOB method should aim. The $eCoB$ is then used together with the CoB of D_1 to compute an orientation in the image plane, referred to as η. Once again by plotting the estimated orientation η with the true one Φ, a relationship can be seen between these quantities, as illustrated in Figure 8. This relationship is represented by the following equation:

$$\Phi(\eta) = a_1 sin(b_1\eta + c_1) + a_2 sin(b_2\eta + c_2) + a_3 sin(b_3\eta + c_3) + a_4 sin(b_4\eta + c_4) \tag{5}$$

The fit error follows a Gaussian distribution with mean $\mu_\Phi = 0.758$ deg and standard deviation $\sigma_\Phi =$

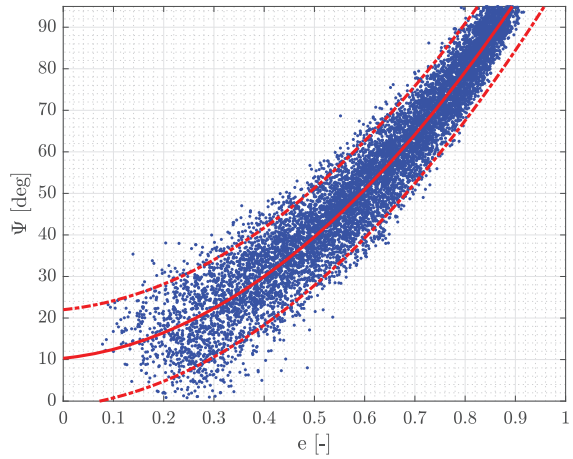

Figure 6: Ψ function (solid red) and 3σ value (dashed red) together with all datapoints of DB_0 (blue).

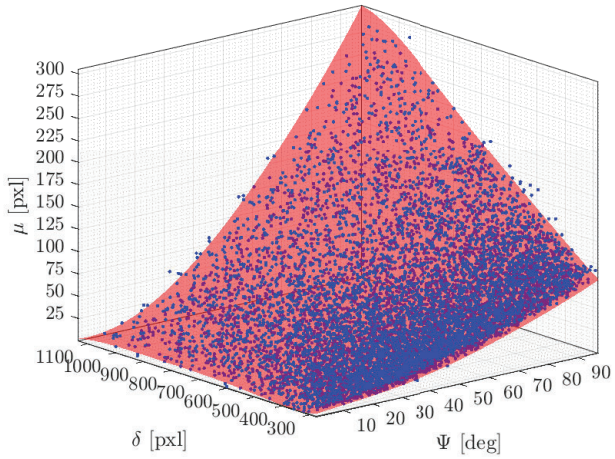

Figure 7: μ function (red surface) vs Ψ and δ for all datapoints of DB_0 (blue).

33.895 deg. The coefficients of the μ, Ψ, and Φ functions are not reported in this work but are the same ones that are used in [18]. Now that both μ and Φ have been computed from the image, they are combined in the following equation:

$$\begin{bmatrix} CoF_x \\ CoF_y \end{bmatrix} = \begin{bmatrix} CoB_x \\ CoB_y \end{bmatrix} + \omega \cdot \mu(\Psi, \delta) \cdot \begin{bmatrix} \cos(\Phi) \\ \sin(\Phi) \end{bmatrix} \tag{6}$$

where ω is a weighting factor that can be used to tune the correction term. It is immediate to understand that when $\omega = 0$ the WCOB degenerates into the COB method. In this work, a value of $\omega = 1$ is used for all geometric conditions, but in general, this parameter could be optimized or varied in real-time depending on the operative conditions. Also, note that at the current stage only synthetic images are used to train the WCOB functions. In future iterations, it would be possible to use real images, as they could be abundantly available from the Hera and DART missions before Milani is released.

SSWCOB

The Sun Sensor WCOB (SSWCOB) is a variant of the WCOB in which the CoB estimate is corrected by a scattering law derived empirically through data for the irregular body considered and from the Sun sensor. As for the WCOB, the main goal of the SSWCOB is to generate a correction vector on the image plane

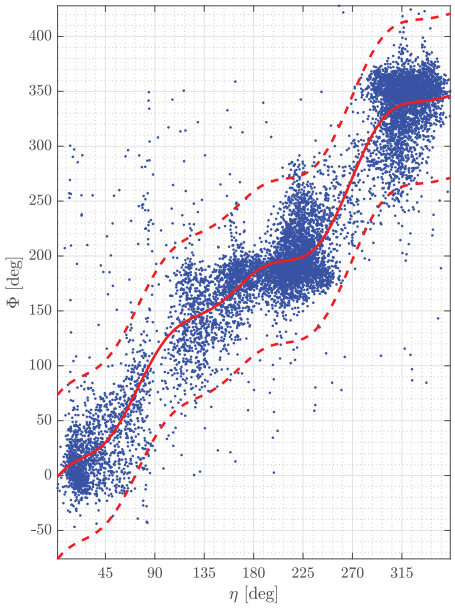

Figure 8: Φ function (solid red) and 3σ value (dashed red) together with all datapoints of DB_0 (blue).

that pushes the CoB towards the CoM. Oppositely from the WCOB, a large portion of the functionalities and quantities extracted from the image are substituted by data from the Sun Sensor. This simplifies the algorithm at the cost of making it dependable on additional sensors. The architecture of the SSWCOB method is illustrated in Figure 9.

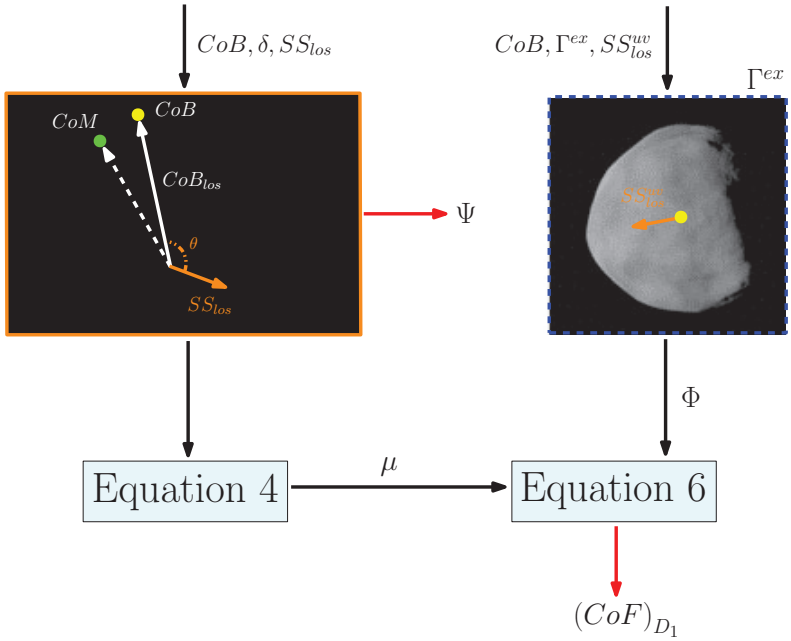

Figure 9: Architecture of the SSWCOB algorithm. The red arrow represents the output of the algorithm.

As for the WCOB algorithm, two pipelines are identified for the determination of μ and Φ. Flowing first from the μ pipeline, data retrieved from the Sun Sensor is used to compute Ψ. The IP receives the line of

sight vector of the Sun direction in the CubeSat reference frame estimated by the Sun Sensor. Using known rigid rotation matrices and assuming to know the attitude quaternion from the ADCS system, the CoB_{los} and SS_{los} are transformed in the same reference frame. The angle θ between these two lines of sights is therefore computed and related to Ψ as:

$$\Psi \approx \pi - \theta \tag{7}$$

This formula is an approximation of Ψ since the computation is performed from the CoB (available from the image) and not from the CoM (unknown at the moment of the estimation). As for the WCOB method, once Ψ is determined, μ is computed by applying Equation 4.

Switching now to the pipeline to compute Φ, the projection of the line of sight of the Sun in the image plane is used, SS^{uv}_{los}. This quantity, centered on the CoB of D_1, is used to provide an orientation from which the angle Φ is computed. Having determined both μ and Φ, the same formula used in the WCOB is now applied to determine the correction term to apply to the CoB of D_1.

RESULTS

The performances of the IP are now tested on the FRP and CRP datasets. First, the performance of the object recognition function within the *Blobs Characterization* block are illustrated, followed up by the ones of the *Observables Extraction* block.

The performance assessment presented in this work is defined as a 'static' one, since it is based on the application of the IP on a datasets generated beforehand. On the other hand, the performance assessment of the WCOB presented in [15] can be considered as a 'dynamic' one, since it is done with the IP and the rest of the GNC system connected in closed-loop.

Blobs Characterization

To assess the performance of the object recognition function to distinguish between D_2 and D_1 in the image, the following metrics have been considered:

$$A = \frac{TP + TN}{TP + FP + TN + FN} \tag{8}$$

$$P = \frac{TP}{TP + FP} \tag{9}$$

$$R = \frac{TP}{TP + FN} \tag{10}$$

where A, P, R stand respectively for accuracy, precision, and recall and TP, TN, FP, FN stands respectively for True Positive, True Negative, False Positive, and False Negative. Since by design all datasets have always D_1 in the images, the metrics are evaluated for the correct detection of D_2.

The performance are summarized in Table 2. First of all, it is possible to see that the conditions in which D_2 is observed in the image are well balanced among the training (DB_0) and testing (FRP and CRP) datasets. Due to the geometrical configuration of D_1, D_2, and Milani several phenomena can occur that impact the visibility of D_2 in the image. In particular, D_2 could be: occluded by D_1, in the shadow region created by D_1, outside of the FOV of the navcam, or in front of D_1 occluding portions of it. Of these scenarios, the latter is the most challenging one for the object recognition algorithm. The relative frequency at which this happens is reported for the three datasets in Table 2, as well as the relative frequency of the other phenomena, which make D_2 not visible by the navcam.

From a performance perspective, it is possible to see that the object recognition is capable to recognize D_2 with high precision (≥ 99.83 in all datasets) but with a medium-high recall ($81.77 \leq R \leq 89.27$). Therefore, the object recognition algorithm is characterized by a low rate of FP and a high rate of FN detection of D_2. This is a consequence of the design of the object recognition algorithm. Note that the algorithm is based on the generation of an expanded bounding box which rejects regions of the terminator of D_1 from being

Table 2: Performance of the object recognition algorithm.

	DB_0	FRP	CRP
Number of images	10000	12102	16020
D_1 is observable [%]	100	100	100
D_2 is observable [%]	80.96	88.88	75.38
D_2 over D_1 [%]	7.56	12.35	13.76
Accuracy	91.20	87.39	86.15
Precision	99.85	99.95	99.83
Recall	89.27	85.86	81.77

wrongly labeled as D_2. This works as expected, but introduces a high rate of FN whenever D_2 is transiting above D_1, as seen from the CubeSat perspective. Having this in mind, and without the desire to complicate the algorithms of the *Observables Exctraction* block to cope with these cases, this behavior is accepted once it has been observed to impact minimally over the performances of the WCOB and SSWCOB algorithms. Indeed, these algorithms seems to be significantly impacted by the disturbance generated by D_2 only when the two asteroids are as far away as possible from each other and their edges are connecting together, generating a combined blob of pixels much greater than expected. Some examples of D_2 recognition are illustrated in Figure 10, together with their associated Γ and Γ^{ex} to exemplify the performance of the algorithm.

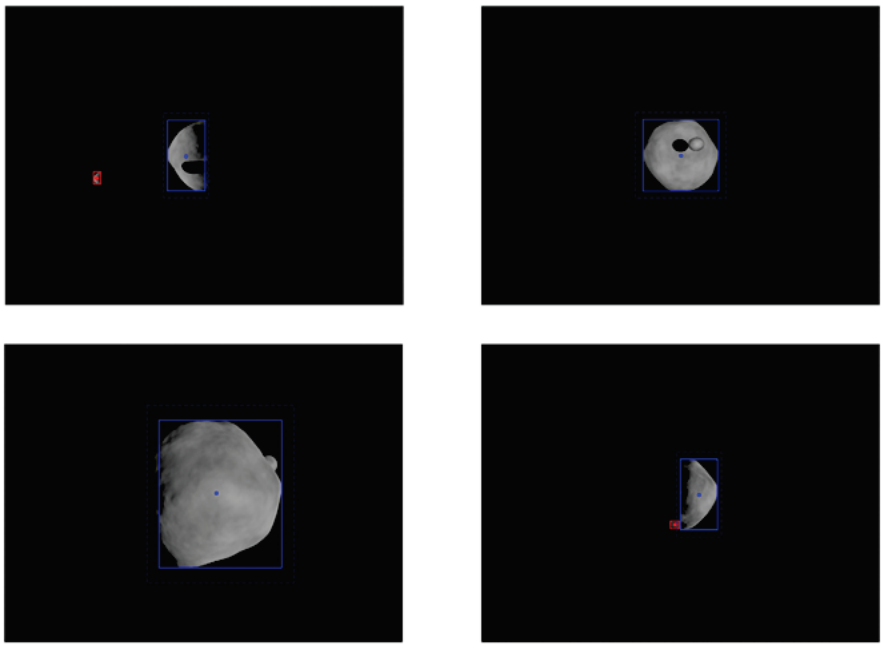

Figure 10: Object recognition examples in the Didymos system. From Top-left to Bottom-right, left to right there are respectively cases of TP, FN, FN, and FP for D_2 detection. The blue and red bounding boxes are the one associated to D_1 and D_2, respectively.

Observables extraction

In this section, the performance of the *Observables Extraction* block of the IP is discussed in detail. The assessment in this work is focused on the $(CoF)_{D_1}$, Ψ, and ρ output of the IP thus excluding the $(CoF)_{D_2}$

from the analysis. It is also remarked that the performance of the SSWCOB is evaluated without introducing any error in the attitude knowledge nor in the line of sight reading from the Sun Sensor, which is therefore modeled as an ideal sensor. This choice has been made to have the SSWCOB being purely evaluated from an IP perspective and at the best of its capability. For a more realistic evaluation its performances shall be modeled with multiple sets of errors both in the attitude and sensor readings. The following error metrics are defined:

$$\varepsilon^x_{CoF} = CoM_x - CoF_x \tag{11}$$

$$\varepsilon^y_{CoF} = CoM_y - CoF_y \tag{12}$$

$$\varepsilon^n_{CoF} = \sqrt{\left(\varepsilon^x_{CoF}\right)^2 + \left(\varepsilon^y_{CoF}\right)^2} \tag{13}$$

$$\varepsilon_\psi = \psi - \psi^t \tag{14}$$

$$\varepsilon_\rho = \rho - \rho^t \tag{15}$$

where the diacritic ^{t} indicates the true value, while the quantities without diacritic are intended to be the ones estimated by the IP.

First, a series of histograms illustrate the distributions of ε^n_{CoF}, ε_Ψ, and ε_ρ in the FRP and CRP datasets. Note that the same color code is used across this section to distinguish the performance of the COB, WCOB, and SSWCOB. From the histograms in Figure 11 it is possible to appreciate the beneficial effect of the data-driven scattering laws of the WCOB and SSWCOB in increasing the accuracy of the CoF estimate. In Figure 12 is possible to see that Equation 7, although an approximation, is capable to estimate Ψ much more accurately than the estimate generated from the image alone. This result has been expected and is reflected in the performance of the WCOB and SSWCOB methods. The greater accuracy which the SSWCOB can exploit to estimate Ψ is also the main reason for the better performance observed in Figure 11: with an accurate Ψ, the resulting μ is estimated better, since both the WCOB and SSWCOB are evaluated over the same δ for each image.

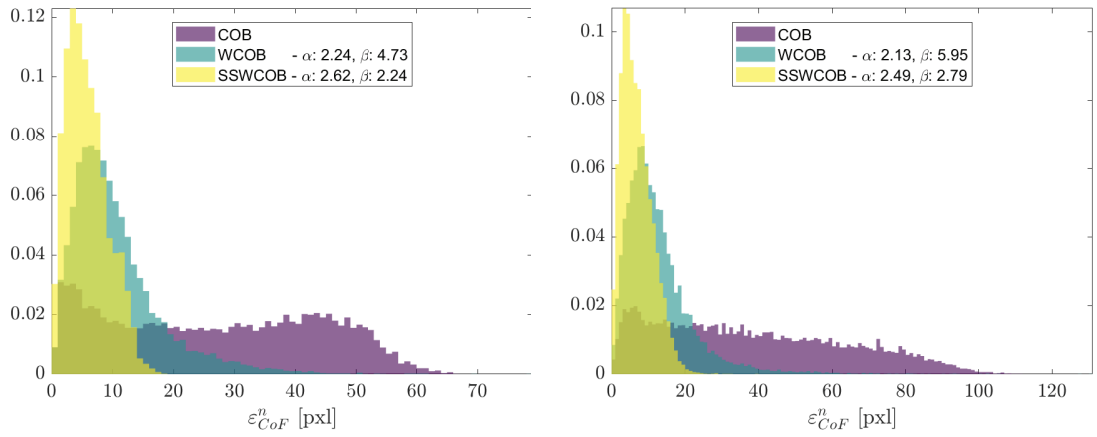

Figure 11: Histograms of the ε^n_{CoF} errors of the COB, WCOB, and SSWCOB in the FRP (left) and CRP (right) datasets. The width of the bins is set to 1 pixel.

Looking at the histograms of ρ in Figure 13, it is possible to see a bias in the error, which is accompanied by a high standard deviation. This results in a noisy reading of the range from the IP which may not be beneficial for use as a standalone quantity (e.g., to trigger an event or another functionality outside of the IP) or in the GNC system. For completeness, all metrics are reported in Table 1 with their means and standard deviations.

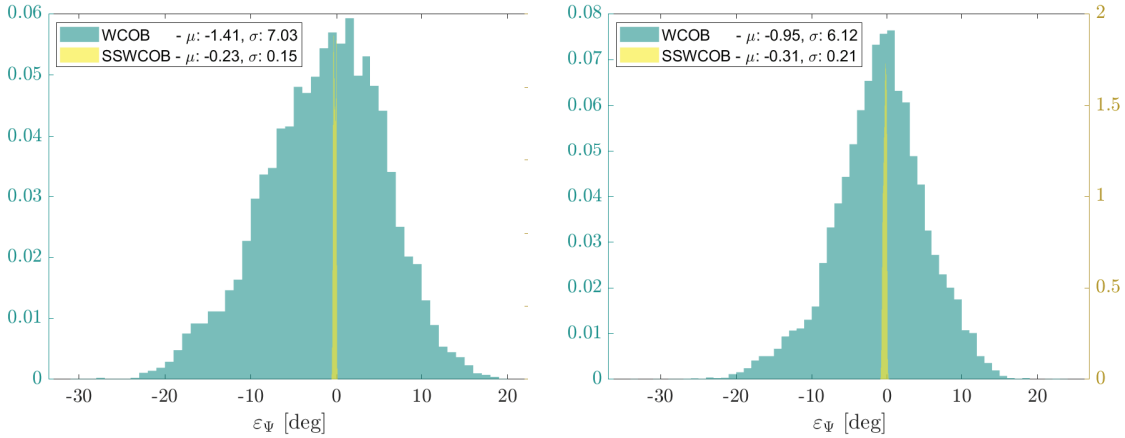

Figure 12: Histograms of the ε_Ψ errors of the WCOB, and SSWCOB in the FRP (left) and CRP (right) datasets. The width of the bins is set to $1°$ and $0.05°$ respectively for the WCOB and SSWCOB.

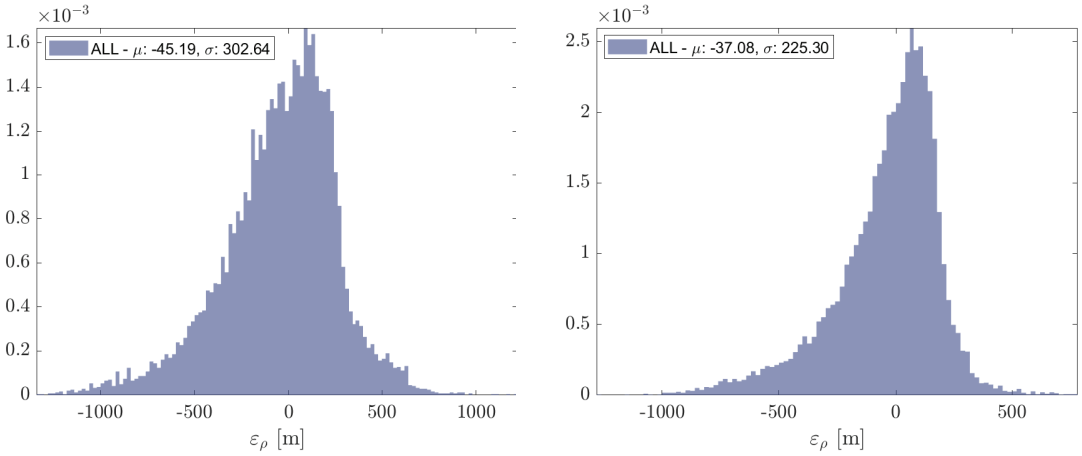

Figure 13: Histograms of the ε_ρ errors in the FRP (left) and CRP (right) datasets. The width of the bins is set to 20 m.

Another interesting visualization of the performance of the IP is visible in Figure 14, which depicts the distributions of ε^x_{CoF} and ε^y_{CoF} in the image plane, together with their error ellipses. It is possible to visually appreciate what the previous histograms have already illustrated: a trend in the increase of the accuracy passing from the COB to the WCOB to the SSWCOB. It is also possible to note the different orientations of the ellipses from FRP to CRP and a bias in the CoF estimate by the COB method in the CRP, which is explained by the nature of its asymmetrical trajectories, as illustrated in Figure 4. The parameters of the error ellipses in Figure 14 are reported for completeness in Table 4.

In Figure 15 and Figure 16 it is possible to see the performance of the COB, WCOB, and SSWCOB as a function of time during the first two arcs of the FRP and CRP phases, together with the values of ρ^t and Ψ^t. Once again, it is possible to note the higher accuracy of the estimate of Ψ by the SSWCOB when comparing it with the one of the WCOB. Moreover, the estimate of Ψ by the WCOB seems to degrade with low values of Ψ^t. This is explained by the poor accuracy of the data-driven function with low values of e (which are associated to lower phase angles), as illustrated in Figure 6. Because both the WCOB and SSWCOB estimates

Table 3: Performance metrics of the COB, WCOB, and SSWCOB in the *FRP* and *CRP* datasets.

		FRP			*CRP*		
	Metric	**COB**	**WCOB**	**SSWCOB**	**COB**	**WCOB**	**SSWCOB**
ε^n_{CoF}	μ [pxl]	27.00	10.60	5.87	38.46	12.69	6.96
	σ [pxl]	17.05	7.08	3.62	25.52	8.69	4.41
ε^x_{CoF}	μ [pxl]	-2.47	1.12	-0.41	-34.70	-0.64	0.66
	σ [pxl]	29.66	7.28	3.71	28.38	8.69	4.73
ε^y_{CoF}	μ [pxl]	-2.22	-2.10	-0.75	-6.74	1.95	-0.58
	σ [pxl]	11.37	10.49	5.58	8.67	13.22	6.52
ε_Ψ	μ [m]	n.a.	-1.41	-0.23	n.a.	-0.95	-0.31
	σ [m]	n.a.	7.03	0.15	n.a.	6.12	0.21
ε_ρ	μ [deg]	-45.19	-45.19	-45.19	-37.08	-37.08	-37.08
	σ [deg]	302.64	302.64	302.64	225.30	225.30	225.30

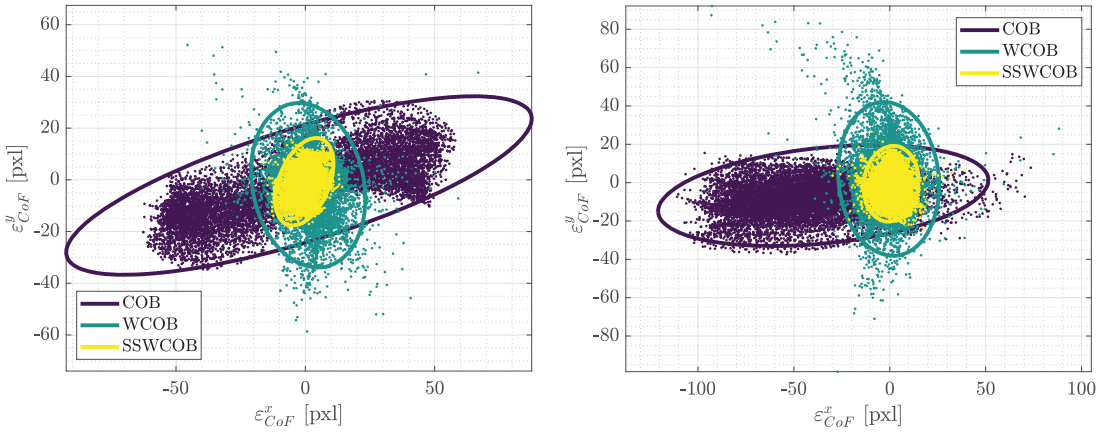

Figure 14: Error ellipses in image plane of ε^x_{CoF} and ε^y_{CoF} for the COB, WCOB, and SSWCOB in the FRP (left) and CRP (right) datasets. A 99% confidence interval is used to draw the ellipses.

the μ term using the same δ extracted from the image, it can be concluded that the overall better accuracy of the SSWCOB against the WCOB method visible in the ε^n_{CoF} error is caused by a better value of Φ, which is orienting the correction term using a more accurate direction. The error on the range is mostly below 1 km and it is observed to vary with ρ^t with an expected trend. It is also noted that such error is affected more from ρ^t than Ψ^t. While for most of the phases low values of Ψ^t are associated to low values of ρ^t and vice-versa, around day 3 of the CRP is clearly visible an interval of time in which this is not true. In this interval the performance of ρ follows the trend driven by ρ^t. Being the range estimated using δ, as described in Equation 1, it is possible to conclude that this parameter is capable to provide a strong estimate in the face of challenging illumination conditions. This is a consequence of a geometric property of the fitted ellipse in the image plane: assuming a constant distance while facing D_1 with varying phase angles, the variability of δ would be small. Finally, from Figure 16 is also possible to see a limitation of data-driven approaches, which shall be considered from an operational point of view: outside their training envelope, the methods cannot be used. Because this scenario may happens, the COB is designed to replace the WCOB and SSWCOB whenever conditions for their applications are not met. Finally, around days 2 and 5.5 of the FRP and days 2.5 and 3.75 of the CRP it is possible to clearly see that the COB method perform better than the others. These events occur whenever low values of Ψ^t are reached.

Figure 17 and Figure 18 illustrate the best method for each phase identified as the one achieving the

Table 4: Parameters of the error ellipses from Figure 14.

	FRP			*CRP*		
Parameter	**COB**	**WCOB**	**SSWCOB**	**COB**	**WCOB**	**SSWCOB**
X_0 [pxl]	-2.47	1.12	-0.41	-34.70	-0.64	0.66
Y_0 [pxl]	-2.22	-2.10	-0.75	-6.74	1.95	-0.58
a [pxl]	93.89	32.20	17.85	86.55	40.23	19.88
b [pxl]	21.86	21.53	9.75	24.92	26.18	14.24
θ [deg]	197.00	101.83	67.87	185.85	95.77	82.31

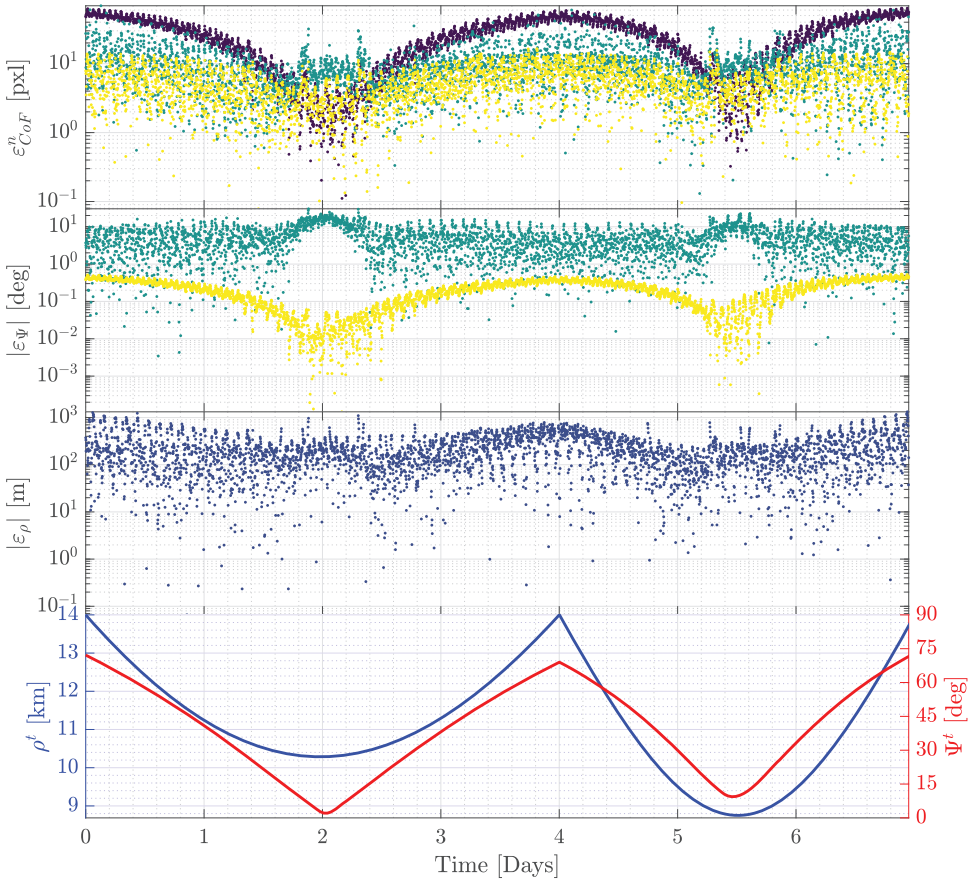

Figure 15: Performances of the COB, WCOB, and SSWCOB as function time during the first two arcs of the FRP.

smallest ε^n_{CoF}. The points on the FRP and CRP datasets associated with the best methods are represented in a phase space together with Ψ^t and ρ^t. In the FRP the COB, WCOB, and SSWCOB are considered the best respectively for 8.71%, 22.94%, and 68.35% of the cases. In the CRP the COB, WCOB, and SSWCOB are considered the best respectively for the 8.18%, 22.18%, and 69.64% of the cases above 4 km. From Figure 17 and Figure 18 is also possible to see a clear preference for the COB method whenever Ψ^t is low. In these cases, the application of a data-driven scattering law seems unfruitful with respect to a simple CoB estimate.

Finally, Figure 19 and Figure 20 attempts to represent the points in space in the DB_0 database in which the WCOB is better than the COB and the SSWCOB is better than the WCOB, using as metric the ε^n_{CoF} errors.

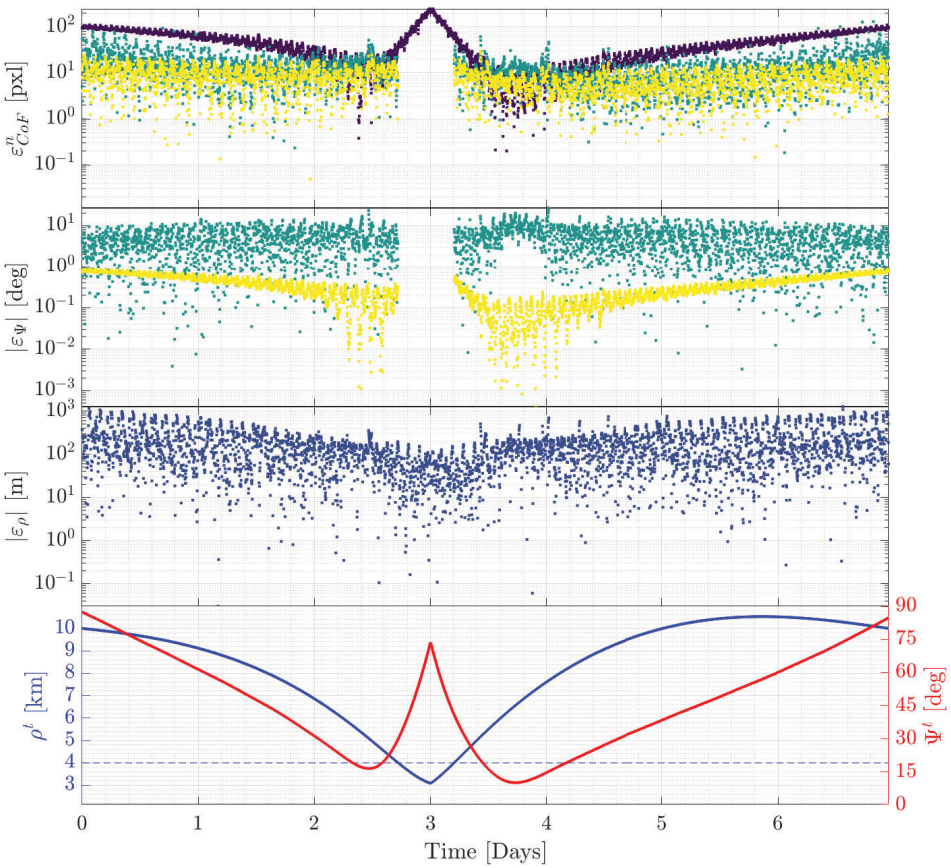

Figure 16: Performances of the COB, WCOB, and SSWCOB as function time during the first two arcs of the CRP. Points below 4 km are omitted for the WCOB and SSWCOB.

From these figures, it is immediately clear once again that the WCOB is exceptional in reducing very large errors in a wide range of phase angles from medium to high, being the illumination from the Sun coming from the X-axis. At the same time it is possible to see that the gain of the SSWCOB over the WCOB is less remarkable if not in the areas at very high phase angles while is being consistently spread across various points in space for smaller improvements.

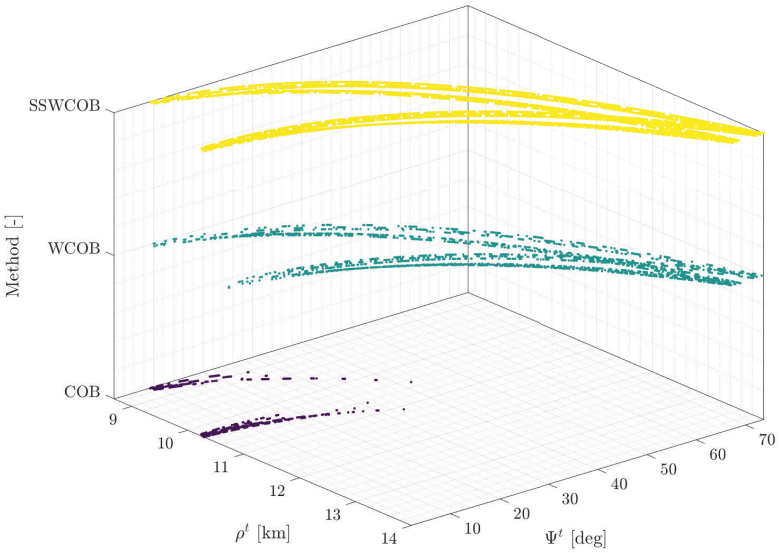

Figure 17: Scatter plot of the method with the smallest ε^n_{CoF} as a function of the range and phase angle in FRP.

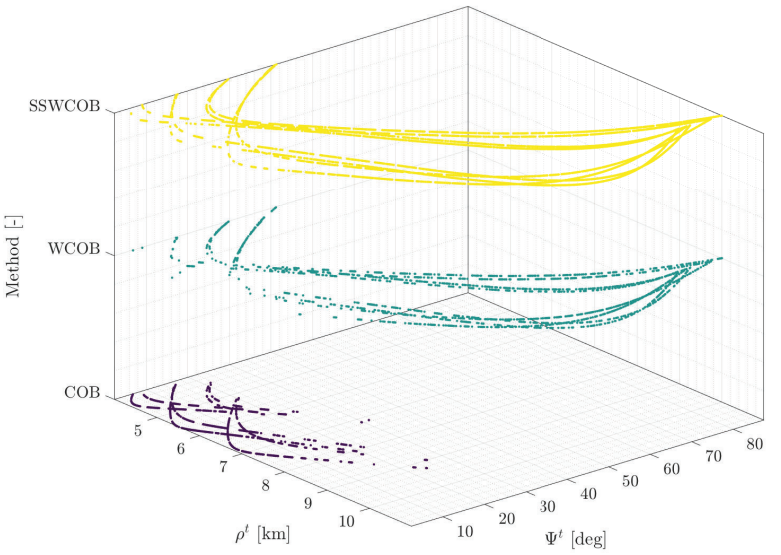

Figure 18: Scatter plot of the method with the smallest ε^n_{CoF} as a function of the range and phase angle in CRP.

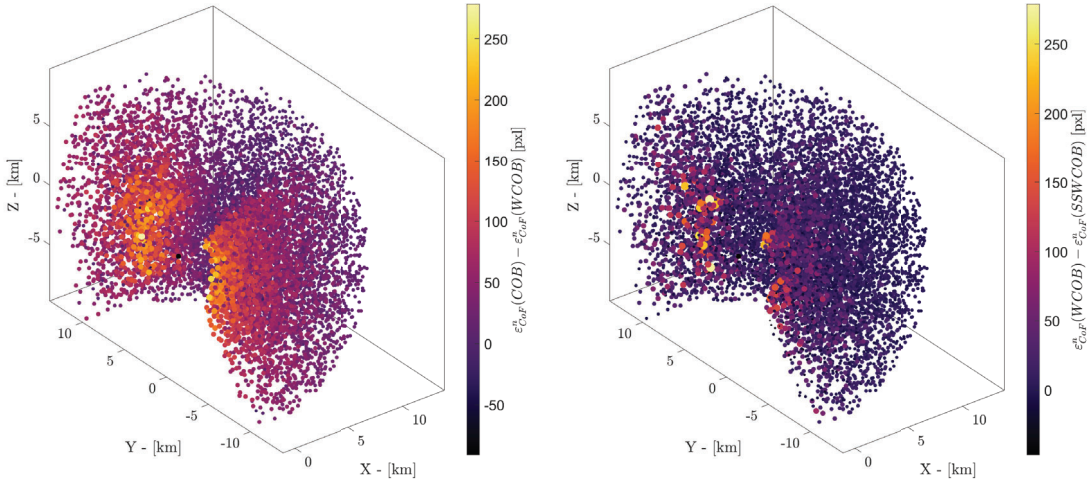

Figure 19: Scatter plot of the error between the COB and WCOB (left) and WCOB and SSWCOB (right) in the DB_0 dataset. The color metric used is the difference between the ε^n_{CoF} errors.

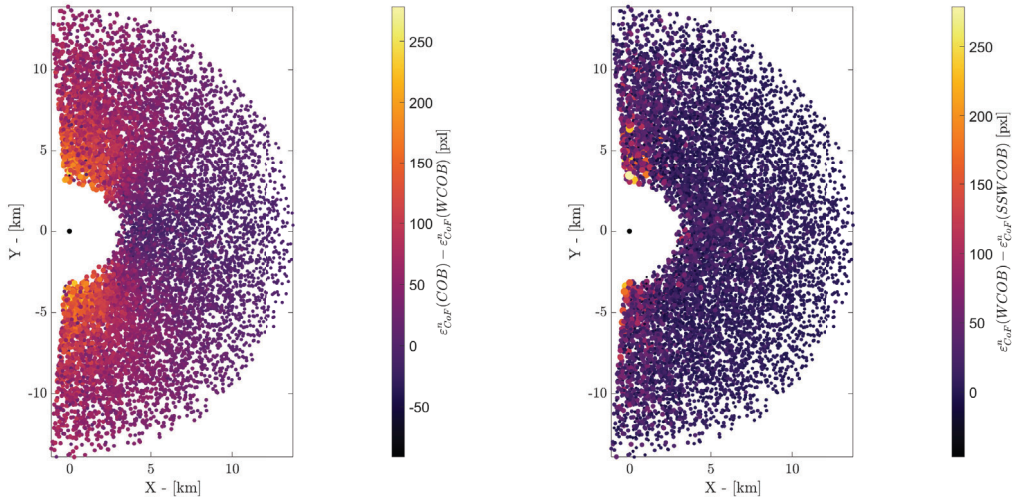

Figure 20: Scatter plot of the error between the COB and WCOB (left) and WCOB and SSWCOB (right) in the DB_0 dataset. The color metric used is the difference between the ε^n_{CoF} errors.

CONCLUSION AND FUTURE WORKS

In this work, for the first time, the design of Milani's image processing is described in detail. The key functionalities of the most important blocks of the IP are tested over the FRP and CRP datasets, which together constitute a total of 28122 images being tested. It is demonstrated that the object recognition function works well in distinguishing D_2 from D_1 whenever the two bodies are separated in the image while it performs poorly whenever D_2 appears in front of D_1 in the image. Nonetheless, in these cases, the failure of the object recognition algorithm does not seem to impact the performance of the observables extraction step of the IP. The latter is constituted by 3 algorithms: the COB, WCOB, and SSWCOB, whose performances are characterized in detail. In particular, their capability to extract the CoF of D_1, the phase angle Ψ and the range ρ from D_1 are tested on the nominal phases of the mission. The analysis carried out in this work demonstrates that the IP can robustly generate a set of observables across the FRP and CRP phases of the mission by exploiting different algorithms. In doing so, the SSWCOB seems to be the most accurate and robust one, followed up by the WCOB and COB. In particular, it is noted that the WCOB method could play the role of backup of the SSWCOB method, while at low phase angles, it would be more beneficial to use the COB method and not apply any scattering law at all in the estimate of the CoF of D_1. Operationally, this could be achieved by a change in the mode of the IP or by a varying ω factor which nullifies or at least reduce the impact of the correction term in the WCOB and SSWCOB formulations. It is also observed that the WCOB would be a perfect backup option in case of a high level of noise in the Sun Sensor readings or high attitude errors from the ADCS, which are expected to degrade the performance of the SSWCOB presented in this work. It is also noted that the range estimated by the IP is often noisy and not accurate, which in the past has been observed to be an issue when transmitted to the GNC.

Future works include a robustness assessment introducing noise in the images, testing the IP with different and more irregular shapes, and most importantly to introduce attitude pointing and Sun sensor errors which will degrade the SSWCOB performance to a level which would be more representative of the real mission.

ACKNOWLEDGMENTS

This work is part of the ESA contract No. 4000131925/20/NL/GLC for the mission phases A/B/C/D/E of Milani. The authors would like to acknowledge the support received by the whole Milani consortium, which is led by Tyvak International. M.P and F.T would like to acknowledge the funding received from the European Union's Horizon 2020 research and innovation programme under the Marie Skłodowska-Curie grant agreement No 813644.

REFERENCES

[1] K.-H. Glassmeier, H. Boehnhardt, D. Koschny, E. Kührt, and I. Richter, "The Rosetta mission: flying towards the origin of the solar system," *Space Science Reviews*, Vol. 128, No. 1, 2007, pp. 1–21. DOI: 10.1007/s11214-006-9140-8.

[2] M. Yoshikawa, J. Kawaguchi, A. Fujiwara, and A. Tsuchiyama, "Hayabusa sample return mission," *Asteroids IV*, Vol. 1, 2015, pp. 397–418. DOI: 10.2458/azu_uapress_9780816532131-ch021.

[3] S.-i. Watanabe, Y. Tsuda, M. Yoshikawa, S. Tanaka, T. Saiki, and S. Nakazawa, "Hayabusa2 mission overview," *Space Science Reviews*, Vol. 208, No. 1, 2017, pp. 3–16. DOI: 10.1007/s11214-017-0377-1.

[4] D. Lauretta, S. Balram-Knutson, E. Beshore, W. Boynton, C. D. d'Aubigny, D. DellaGiustina, H. Enos, D. Golish, C. Hergenrother, E. Howell, *et al.*, "OSIRIS-REx: sample return from asteroid (101955) Bennu," *Space Science Reviews*, Vol. 212, No. 1, 2017, pp. 925–984. DOI: 10.1007/s11214-017-0405-1.

[5] C. Snodgrass and G. H. Jones, "The European Space Agency's comet interceptor lies in wait," *Nature communications*, Vol. 10, No. 1, 2019, pp. 1–4. DOI: 10.1038/s41467-019-13470-1.

[6] P. Michel, M. Küppers, and I. Carnelli, "The Hera mission: European component of the ESA-NASA AIDA mission to a binary asteroid," *COSPAR Scientific Assembly*, Pasadena, California, 2018, pp. 1–42.

[7] H. F. Levison, C. B. Olkin, K. S. Noll, S. Marchi, J. F. B. III, E. Bierhaus, R. Binzel, W. Bottke, D. Britt, M. Brown, M. Buie, P. Christensen, J. Emery, W. Grundy, V. E. Hamilton, C. Howett, S. Mottola, M. Pätzold, D. Reuter, J. Spencer, T. S. Statler, S. A. Stern, J. Sunshine, H. Weaver, and I. Wong, "Lucy Mission to the Trojan Asteroids: Science Goals," *The Planetary Science Journal*, Vol. 2, Aug. 2021, p. 171, 10.3847/psj/abf840.

[8] R. Walker, D. Binns, C. Bramanti, *et al.*, "Deep-space CubeSats: thinking inside the box," *Astronomy & Geophysics*, Vol. 59, No. 5, 2018, pp. 5–24. DOI: 10.1093/astrogeo/aty237.

[9] P. Michel, A. Cheng, and M. Küppers, "Asteroid Impact and Deflection Assessment (AIDA) mission: science investigation of a binary system and mitigation test," *European Planetary Science Congress*, Vol. 10, 2015, pp. 123–124.

[10] J. A. Atchison, M. T. Ozimek, B. L. Kantsiper, and A. F. Cheng, "Trajectory options for the DART mission," *Acta Astronautica*, Vol. 123, 2016, pp. 330–339. DOI: 10.1016/j.actaastro.2016.03.032.

[11] E. Dotto, V. Della Corte, M. Amoroso, I. Bertini, J. Brucato, A. Capannolo, B. Cotugno, G. Cremonese, V. Di Tana, I. Gai, *et al.*, "LICIACube-the Light Italian Cubesat for Imaging of Asteroids in support of the NASA DART mission towards asteroid (65803) Didymos," *Planetary and Space Science*, 2021, p. 105185. DOI: 10.1016/j.pss.2021.105185.

[12] H. Goldberg, O. Karatekin, B. Ritter, *et al.*, "The Juventas CubeSat in Support of ESA's Hera Mission to the Asteroid Didymos," *Small Satellite Conference*, Logan, Utah, 2019, pp. 1–7.

[13] F. Ferrari, V. Franzese, M. Pugliatti, C. Giordano, and F. Topputo, "Preliminary mission profile of Hera's Milani CubeSat," *Advances in Space Research*, Vol. 67, No. 6, 2021, pp. 2010–2029. DOI: 10.1016/j.asr.2020.12.034.

[14] F. Ferrari, V. Franzese, M. Pugliatti, C. Giordano, and F. Topputo, "Trajectory Options for Hera's Milani CubeSat Around (65803) Didymos," *The Journal of Astronautical Sciences*, Sept. 2021, 10.1007/s40295-021-00282-z.

[15] M. Pugliatti, A. Rizza, F. Piccolo, V. Franzese, C. Bottiglieri, C. Giordano, F. Ferrari, and F. Topputo, "The Milani mission: overview and architecture of the optical-based GNC system," *Scitech 2022*, 2-7 Jan 2022. DOI: 10.2514/6.2022-2381.

[16] T. Kohout, M. Cardi, A. Näsilä, E. Palomba, F. Topputo, and t. Milani team, "Milani CubeSat for ESA Hera mission," *European Planetary Science Congress 2021*, EPSC2021-732, 13–24 Sep 2021. DOI: 10.5194/epsc2021-732.

[17] F. Dirri, E. Palomba, A. Longobardo, D. Biondi, A. Boccaccini, A. Galiano, E. Zampetti, B. Saggin, D. Scaccabarozzi, and J. Martin-Torres, "VISTA Instrument: A PCM-Based Sensor for Organics and Volatiles Characterization by Using Thermogravimetric Technique," *2018 5th IEEE International Workshop on Metrology for AeroSpace (MetroAeroSpace)*, IEEE, jun 2018. DOI: 10.1109/metroaerospace.2018.8453532.

[18] M. Pugliatti, V. Franzese, and F. Topputo, "Data-Driven Image Processing for Onboard Optical Navigation Around a Binary Asteroid," *Journal of Spacecraft and Rockets*, Jan. 2022, pp. 1–17. Article in Advance, 10.2514/1.a35213.

[19] F. Piccolo, M. Pugliatti, P. Panicucci, and F. Topputo, "Toward verification and validation of the Milani Image Processing pipeline in the hardware-in-the-loop testbench TinyV3RSE," *AAS/GNC 2022*, 4-9 Feb 2022.

[20] C. Bottiglieri, F. Piccolo, A. Rizza, C. Giordano, M. Pugliatti, V. Franzese, F. Ferrari, and F. Topputo, "Trajectory design and orbit determination of Hera's Milani CubeSat," *2021 AAS/AIAA Astrodynamics Specialist Conference*, Big Sky, Montana, 2021, pp. 1–15.

[21] N. Otsu, "A Threshold Selection Method from Gray-Level Histograms," *IEEE Transactions on Systems, Man, and Cybernetics*, Vol. 9, No. 1, 1979, pp. 62–66, 10.1109/TSMC.1979.4310076.

[22] S. Bhaskaran, J. E. Riedel, and S. P. Synnott, "Autonomous nucleus tracking for comet/asteroid encounters: the Stardust example," 1998.

[23] C. Wright, A. J. Liounis, and B. Ashman, "Optical navigation algorithm performance," 2018. 1st Annual RPI Workshop on Image-Based Modeling and Navigation for Space Applications, Troy, NY.